JOURNAL OF MATERIALS SCIENCE **33** (1998) 117–131

Anisotropic etching of silicon crystals in KOH solution

Part III *Experimental and theoretical shapes for 3D structures micro-machined in (hk0) plates*

C. R. TELLIER
Laboratoire de Chronométrie, Electronique et Piézoélectricité, Ecole Nationale Supérieure de Mécanique et des Microtechniques, 26 Chemin de l'Epitaphe, 25030 Besancon Cedex, France

The micro-machining of various (*h k 0*) silicon plates in an aqueous KOH solution was studied. Orientation effects, the formation of limiting facets and concave or convex undercuttings have been analysed for (*h k 0*) membranes and mesa obtained starting with circular masks. Procedures have been derived to predict *3D* etching shapes using a tensorial model for the chemical etching. Predicted shapes for membranes have been found to closely agree with experimental shapes because of the important role played by limiting {1 1 1} facets. Theoretical general shapes for etched mesa were also in crude accord with experiments. Consequently some attempts have been made to identify limiting (*h h l*) planes which can participate to convex undercutting and to discuss the role of the dissolution slowness surface.

1. Introduction

In the last decade mechanical sensors [1–8] have often been made with micro-machining techniques from silicon crystals [1–6] or from quartz crystals [7, 8]. Anisotropic etchants are mainly used to fabricate small mechanical structures such as membranes and cantilevers [4, 6, 9]. An anisotropic etching technique produces a fine structure which is often bordered by limiting crystal planes [10–14]. In particular the sharp transition from a crystal plane to another limiting plane causes a thin etched diaphragm which is very fragile. Moreover in most cases anisotropic etching results in convex corner undercutting [13, 14]. This is an effect one attempts to prevent for structures such as mechanical structures involved in silicon based accelerometers. This sharpness of edges as well as the extent of the corner undercutting or of lateral underetching depend essentially on the orientation of the etched plane and of the directions of alignment of the mask pattern [8, 10, 12].

Most silicon-integrated pressure sensors are piezoresistive sensors [1, 2, 5, 6, 15, 16] which consist of a rectangular silicon diaphragm with a bridge of strain gauges. However recently attempts have been made to develop sensors composed of a single element with four terminals arranged like a Hall element [17]. The sensitivity of these new sensors depends mainly on the values for the piezoresistance coefficients as measured in the rotated system [15, 18, 19]. In practice an optimum design of silicon sensors can thus require the micro-machining of structures in wafers whose orientations differ from those ({1 0 0}) or {1 1 0} planes) commonly used in the semiconductor industry. Moreover, turning our attention to the micro-machining of quartz crystals, it is obvious that the metrological performance of thin quartz resonators requires us to start with some specific singly-rotated or doubly-rotated quartz plates such as AT-cuts or SC-cuts [20, 21] in order to minimize temperature effects. Thus for the design of a silicon or quartz sensor we need a model which allows us to predict in three dimensions the exact geometry of micro-machined mechanical structures.

In the recent past several attempts [22–25] have been made to propose graphical simulations of etching shapes. Most of these predictions seem to be based on geometrical constructions and involve only planar limiting facets associated with extrema in the etch rate. Moreover, they frequently can only be applied to the micro-machining of {1 0 0} or {1 1 0} silicon planes. However Tellier *et al.* [12, 26–32] has recently shown that starting from an analytical equation for the dissolution slowness surface of crystals it is possible to derive a three-dimensional simulation of micro-machined structures, especially for silicon.

This paper constitutes part III of a research programme devoted to the etching of $(h\bar{k}0)$ silicon planes in KOH solutions. In this paper we present new experimental results on the micro-machining of thick membranes and mesa in $(h\bar{k}0)$ silicon wafers covered with circularly shaped masking patterns. Emphasis is placed on the role played by the limiting facets in the geometrical features of the final micromechanical structure. We also develop numerical procedures to predict and analyse 3D dissolution shapes starting from the analytical expression of the dissolution slowness surface for silicon crystal previously proposed in part I.

0022–2461
© *1998 Chapman & Hall*

2. Experimental results

2.1. Experimental details

Differently-oriented silicon wafers were cut from a P-type silicon ingot with a resistivity of about 10 Ω cm. The slices are singly-rotated wafers (Fig. 1a) corresponding to the various $(h \bar{k} 0)$ wafers that are listed in Table I. The angle of cut, φ_0, covers a sector of 45°. Prior to etching the wafers were optically polished and then covered with a thermally oxidized silicon oxide film (about 120 nm thick) for passivation. In order to collect sufficient data on the anisotropy of the dissolution process masking patterns of an initially circular shape were used.

TABLE I Values for the angle of cut, φ_0, of singly rotated $(h \bar{k} 0)$ plates

Cuts	$1\bar{6}0$	$1\bar{4}0$	$3\bar{7}0$	$2\bar{3}0$
φ_0 (deg)	9.5	14	23.2	33.7

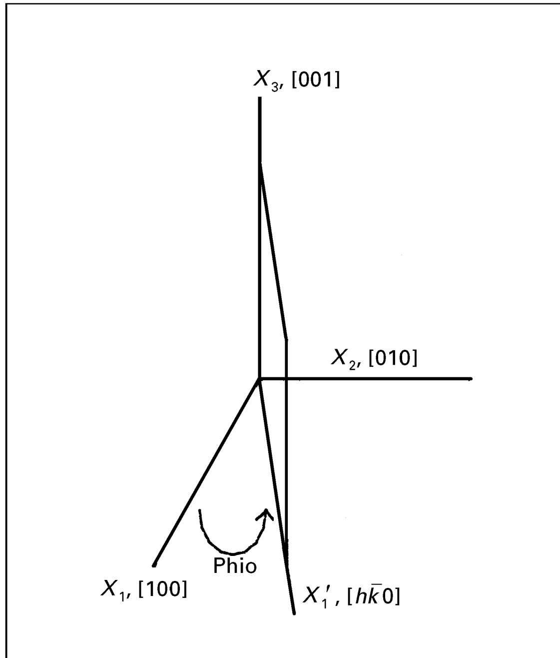

(a)

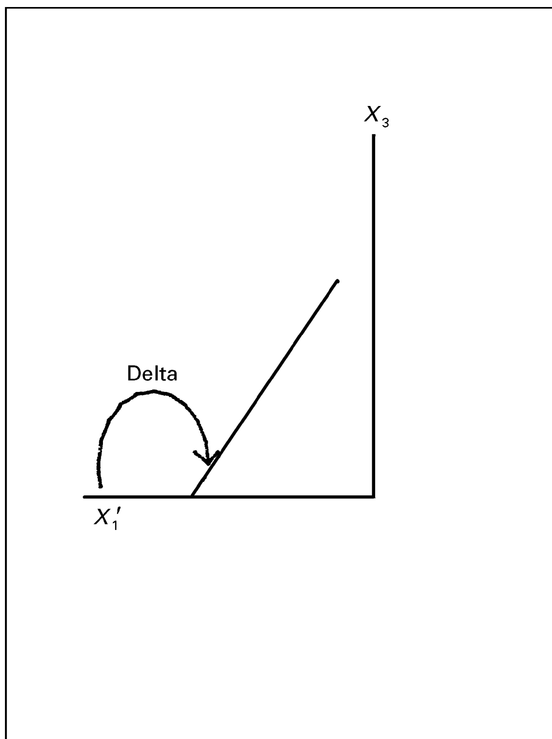

(b)

Figure 1 Geometry of the model (a) Definition of the angle of cut φ, (b) Definition of the angle δ that an intersecting line makes with the rotated axis x_1'.

The pattern was transferred to the passivation layer using a conventional photolithographic process [10]. The wafers were etched in a 35% KOH solution maintained at $60 \pm 0.5\,^{\circ}$C. Care has been taken to keep the concentration of the etchant constant by recondensing the vapours in a water cooled reflux condenser. After etching, diaphragm- or mesa-like structures were observed using scanning electron microscopy (SEM) at a low accelerating voltage (typically 5 kV) and with an observation angle of 0°.

2.2. Membrane-like structures

Visual inspection of the SEM micrographs displayed in Fig. 2(a–d) reveals the significance of the anisotropy of the dissolution process. First of all etched structures satisfy the symmetry of the crystal. Let us recall that the (0 0 1) plane constitutes a cross-sectional plane which intersects the basal $(h k 0)$ plane along the rotated axis, x_1' (Fig. 1b). Then if the etching is only governed by orientation, the (001) plane acts a "minor plane". It is clear from Fig. 2(a–d) that this requirement is fulfilled. Secondly the general shape of all etched structures differs markedly from the starting circular shape. In particular as has been previously observed by several workers [9, 33–35] we obtain a somewhat square shaped diaphragm where $\{1\,1\,1\}$ planes which have the lowest etch rate form lateral sidewalls when we etch a (0 1 0) silicon plane (Fig. 2a).

Only the four corners seem to be bordered by other approximately flat facets. Effectively when we start with a circular pattern of finite radius all surface elements potentially present at the starting surface can participate in the final etched structure. Then provided the etch depth does not reach a critical value, surface elements with a higher etch rate can contribute to the micro-machined membrane. When the angle of cut, φ_0, increases from 0 to 34° we observe a progressive transformation of the squared etching shape ((0 1 0) plane) which becomes continuously elongated with increasing φ_0. The four $\{1\,1\,1\}$ bevelling planes are still present but the extent of two of the $\{1\,1\,1\}$ facets grows at the expense of the other two $\{1\,1\,1\}$ planes (compare Fig. 2d with Fig. 2a for example). It clearly appears (Fig. 2(b–d)) that structures are also bounded by planes which differ from $\{1\,1\,1\}$ planes. Moreover a careful examination of the SEM micrographs (Fig. 2(c and d) reveals that somewhat curved regions (denoted CR on the micrographs) also contribute to the sidewalls. These regions are composed of a succession

Figure 2 SEM micrographs of membranes micro-machined on various singly-rotated plates (a) (0 1 0) plate, (b) $(1\,\bar{6}\,0)$ plate, (c) $(3\,\bar{7}\,0)$ plate, (d) $(2\,\bar{3}\,0)$ plate.

of slightly misoriented planes and appear to be very smooth and free of dissolution figures in contrast with the geometrical features of some limiting facets. Effectively atomic steps or microscopic surface defects induce the development of dissolution figures which are characteristic to the orientation of the facet on which they are formed [10, 30, 31, 36]. Such surface features of planes limiting micro-machined structures allow us to recognize without ambiguity the crystal planes which contribute to the final structure. For example etch figures composed of somewhat vertical steps develop on $\{1\,1\,1\}$ facets (see for example Fig. 2(a–d)).

In contrast a higher magnification micrograph of the right sidewall of the $(2\bar{3}0)$ diaphragm, Fig. 3, reveals the presence of a smooth shoulder (CR) characterized by the absence of any textured surface. This behaviour is probably attributable to the formation of a slightly curved region which here joins the masked surface to the bottom of the thick membrane. Note also that the bottom is covered with typical etch figures [31] which have been identified in part I of this series of papers. In some cases (see Fig. 2d for example) the curved region CR intersects flat $\{1\,1\,1\}$ facets which develop under the mask. Moreover for the $(1\,\bar{6}\,0)$ plate (Fig. 2b) the curved region CR remains slightly misoriented with respect to the reference surface. Moreover in practice the average orientation of

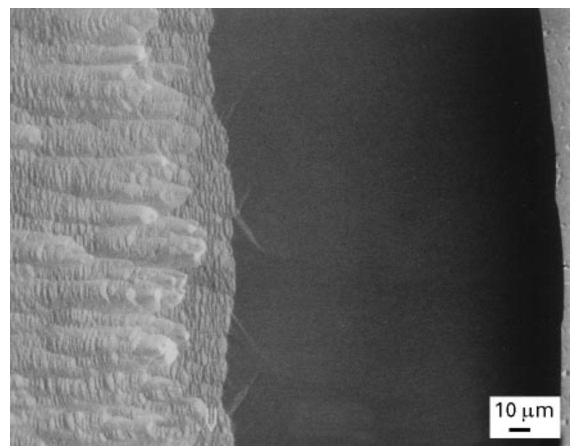

Figure 3 Magnification of the curved sidewall formed on a $(3\,\bar{7}\,0)$ etched membrane.

the region CR remains close to that related to $\{1\,0\,0\}$ planes.

At this point it should be noted that in some directions the sidewalls seem to be associated with sharp cross-sectional dissolution profiles which penetrate to varying extents within the crystal under the mask. Such cross-sectional profiles, which can be qualified as sharp profiles (SP), are clearly depicted on $(1\,\bar{6}\,0)$,

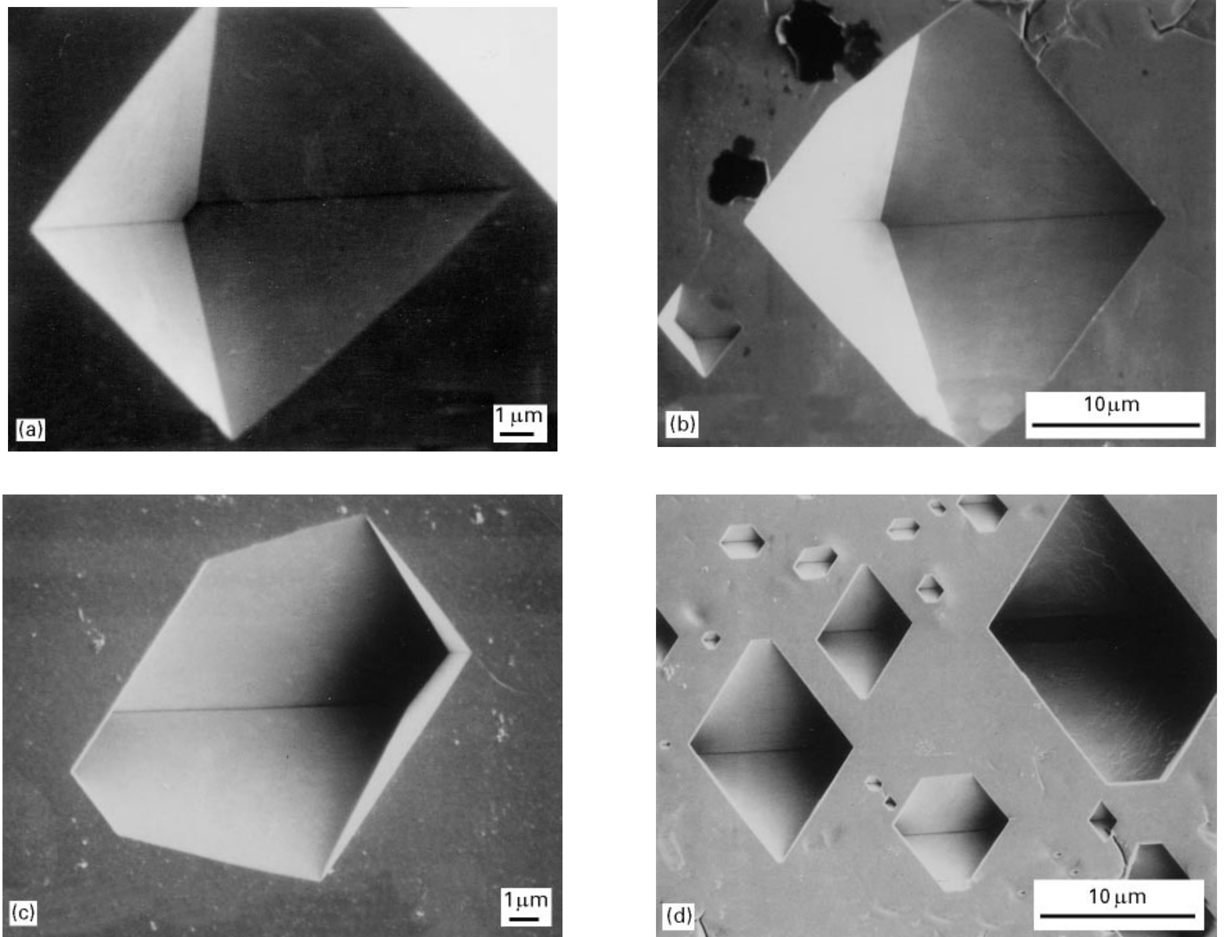

Figure 4 Etched shapes of pin-holes formed on various singly-rotated plates for (a) $(1\,\bar{6}\,0)$, (b) $(1\,\bar{4}\,0)$, (c) $(2\,\bar{3}\,0)$ and (d) $(1\,\bar{1}\,0)$ plates.

$(3\,\bar{7}\,0)$ and $(2\,\bar{3}\,0)$ etched wafers (see regions SP_1, SP_2 and SP_3 in Fig. 2(b–d). Whilst it remains easy to detect the presence of sharp profiles it appears virtually impossible to determine the angle that curved regions and/or limiting facets make when forming a sharp edge.

It may also be of interest to follow the change in the shape for etched holes in the particular case where the initial radius of the circular hole tends to zero. Such an investigation can be conveniently achieved by observation of the so-called pin-holes whose origin is the presence of very small defects in the passivation layer. It is well-known [10, 37] that the etching shape of the pin-holes is essentially determined by preferential limiting planes corresponding to maxima maximora in the dissolution slowness, L. For silicon crystals and a KOH etchant, pin-holes must be bounded by $\{1\,1\,1\}$ planes. This is the reason why pyramidal pin-holes whose sides are aligned along $\langle 1\,1\,0 \rangle$ directions are obtained for a $\{1\,0\,0\}$ reference surface. Fig. 4(a–d) presents etching shapes of the pin-holes formed on various $(h\,\bar{k}\,0)$ surfaces. As the angle of cut, φ_0, varies from 0 to 14° we observe progressive changes in the initial pyramidal shape of the pin-holes which nevertheless are composed of four $\{1\,1\,1\}$ facets. As φ_0 approaches 45° the two bevelling $\{1\,1\,1\}$ planes tend to become orthogonal to the basal $(h\,\bar{k}\,0)$ surface. As a result the etched pin-hole seems to be limited by the two least inclined $\{1\,1\,1\}$ facets (see Fig. 4c for example), the two other $\{1\,1\,1\}$ facets forming sharp edges. Moreover in the SEM micrograph Fig. 4d related to a $(1\,1\,0)$ wafer we observe that the etched pin-hole intersects the reference surface along directions corresponding to the intersection lines for $\{1\,1\,1\}$ limiting planes. Let δ_{mi} be the angle of alignment that an intersecting line, L_i, makes with the rotated axis, x'_1 (Fig. 1b). Table II gives experimental values of the alignment angle for the main intersecting lines.

TABLE II Experimental values for the two angles δ_{mi} determining the main intersections of $\{1\,1\,1\}$ facets with the reference surface $(h\,\bar{k}\,0)$ (here we take into account the mirror effect of the $(0\,0\,1)$ plane)

Plane $(h\,\bar{k}\,0)$	δ_{m1} (deg)	δ_{m2} (deg)
$1\,\bar{6}\,0$	138	50
$1\,\bar{4}\,0$	130	52
$2\,\bar{3}\,0$	124	54
$1\,\bar{1}\,0$	122	56

2.3. Mesa-like structures

Various SEM images of mesa etched in differently-oriented $(h\,\bar{k}\,0)$ planes are displayed in Fig. 5(a–f). All etching shapes display symmetry properties that are specific to the class *m*3*m*. Mesa etched into a $(0\,1\,0)$

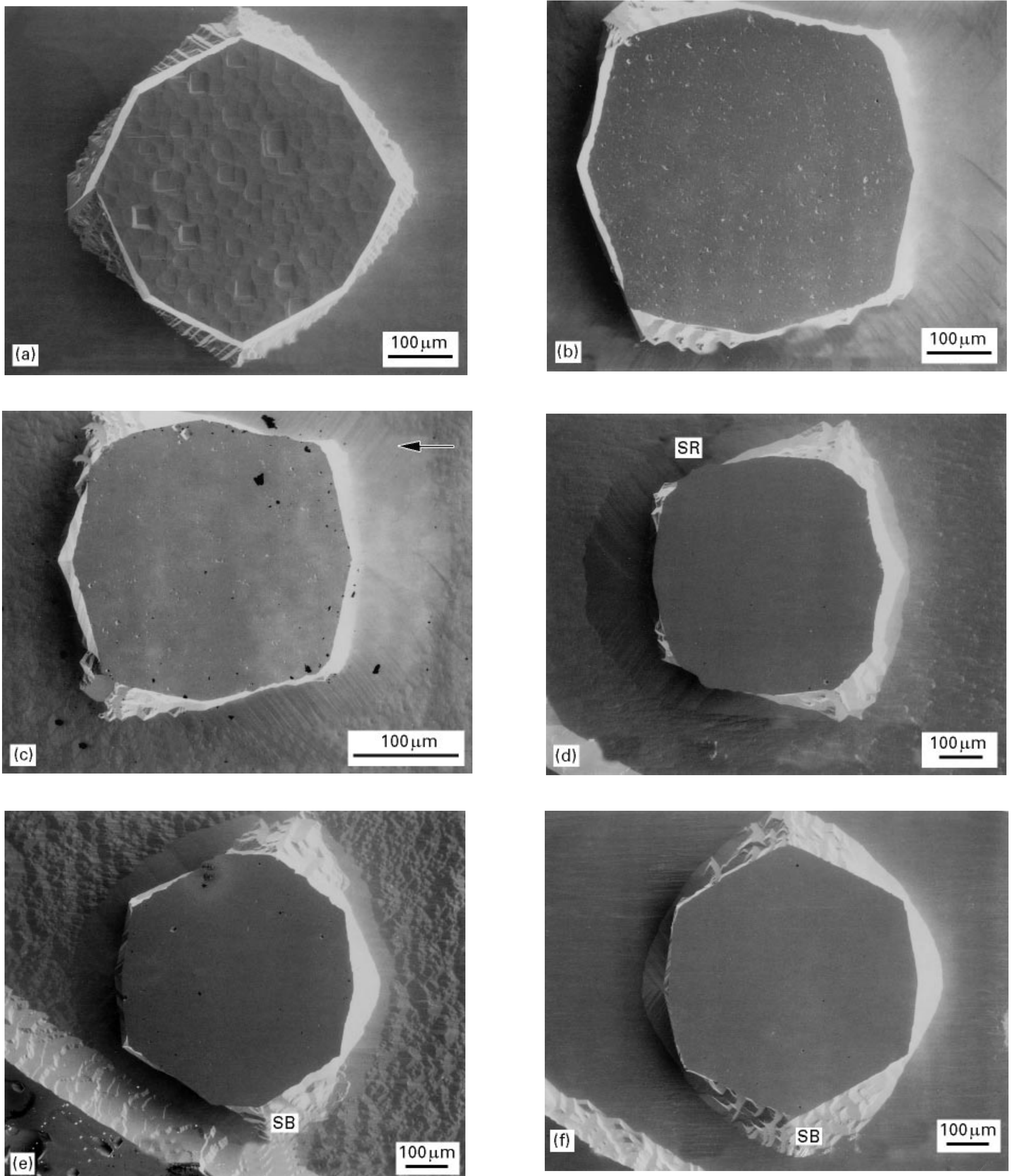

Figure 5 Final shapes for mesa etched on various singly rotated plates for (a) $(0\bar{1}0)$, (b) $(6\bar{1}0)$, (c) $(4\bar{1}0)$, (d) $(7\bar{3}0)$, (e) $(3\bar{2}0)$ and (f) $(1\bar{1}0)$ plates.

wafer exhibit a four-fold symmetry with respect to the $[0\bar{1}0]$ crystallographic axis. In Fig. 5f we recognize the two *m* symmetries associated with the two planes which act as reflection planes namely the (0 1 1) and (1 1 0) planes. For cuts other than $(0\bar{1}0)$ and $(1\bar{1}0)$ cuts the only effect is the "mirror effect" caused by the cross-sectional (0 0 1) plane.

Another important feature which emerges from the SEM micrographs of Fig. 5(a–f) is the point that the initial circular shape of the masking pattern is not preserved after prolonged etching. In reality the general shape of the etched mesa deviates markedly from the starting circular shape because of an important convex undercutting which affects all the $(h\bar{k}0)$ wafers. This behaviour closely agrees with previous observations for mesa-type structures etched in $\{100\}$ wafers [13, 14] and with preliminary theoretical predictions [12] related to the micro-machining of "convex" structures.

Let us now turn our attention to the sidewalls of etched mesa. For this purpose care must be taken that for the $(1\bar{6}0)$ and $(1\bar{4}0)$ mesa the direction of the rotated axis is inverted with respect to $(3\bar{7}0)$ and $(2\bar{3}0)$ planes. In this condition we can follow the progressive appearance of a slightly inclined shoulder (at the right of the $(1\bar{6}0)$ mesa (Fig. 5b)

whose extent diminishes with increasing values of the angle of cut. Magnification of this region (Fig. 6) provides evidence for the total absence of dissolution figures. Thus we can conclude that the wet etching causes the formation of a slightly curved shoulder at the right base of $(1\,\bar{6}\,0)$ and $(1\,\bar{4}\,0)$ mesa (Fig. 5(b and c)). In contrast a linearly textured convex background develops on the bevel which on the left of the mesa joints the unmasked $(3\,\bar{7}\,0)$ plane as demonstrated by the magnified SEM image shown in Fig. 7. Consequently we can infer that as φ_0 reaches 23° the mesa becomes partly surrounded by a limiting plane which for convenience, at this point is designated plane LP1. This limiting plane LP1 appears (Fig. 5(e and f)) to also constitute portions of the sidewalls of $(2\,\bar{3}\,0)$ and $(1\,\bar{1}\,0)$ mesa. Moreover as observed for micro-machined holes the curved regions and/or flat facets bounding etched mesa also make sharp edges in some specific regions identified by the letters "SR" on the various micrographs of Fig. 5(a–f). In general the lateral underetching corresponding to these sharp cross-sectional profiles remains very significant.

It is also of interest to note that some sidewalls appear to be terraced. This behaviour is characteristic of the micro-machining of mechanical structures from masks of an initially convex nature. Fig. 8(a and b) are magnified views of such fragmented sidewalls for two differently oriented reference surfaces. A careful examination of these images reveals that the terraces are composed of three different limiting planes, designated as planes LP1, LP2 and LP3, which are covered by typical dissolution figures. The geometrical features of the etched terraces allow us to identify easily two of these planes as being respectively the $\{1\,1\,1\}$ plane (LP2 plane) and the $\{1\,1\,0\}$ plane (LP3 plane). We can easily recognize the linear texture which develops and $\{1\,1\,0\}$ planes (Part I, [31]) characterized by grooves aligned along $\langle 1\,1\,0 \rangle$ directions. Moreover on the last plane etch figures are formed whose features are identical to figures relative to the limiting plane LP3.

At this point we must take into account that a $\{1\,1\,1\}$ plane corresponds to a maximum maximorum of the dissolution slowness vector, L, and a $\{1\,1\,0\}$ facet to a relative maximum [31]. Thus it seems reasonable at first sight to infer that the plane LP3 is also correlated to a maximum in L. Note that the preceding observations related to terraced sidewalls and the conclusion drawn from these observations depart from the assumption commonly made [38] on the active participation of planes associated with minima in L.

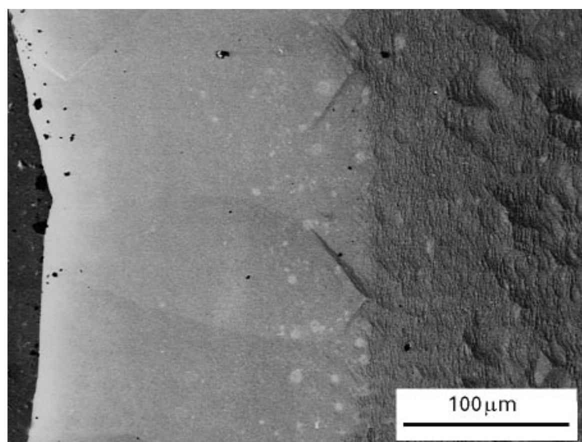

Figure 6 Magnification of the curved sidewall which develops, on the right region of a mesa etched on a $(1\,\bar{4}\,0)$ plate.

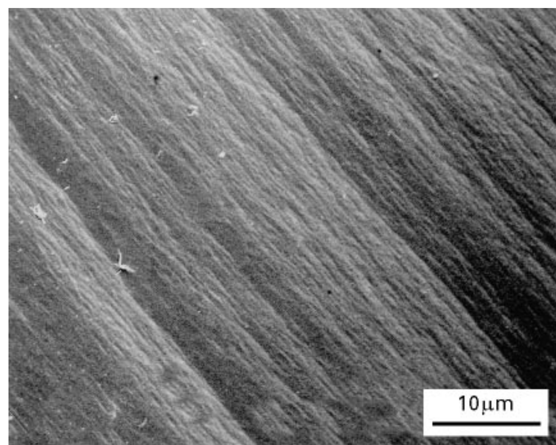

Figure 7 Magnification of the bevelling plane which develops on the left side of a $(3\,\bar{7}\,0)$ mesa.

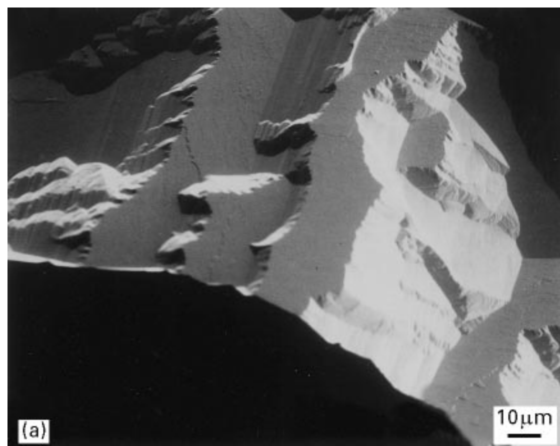

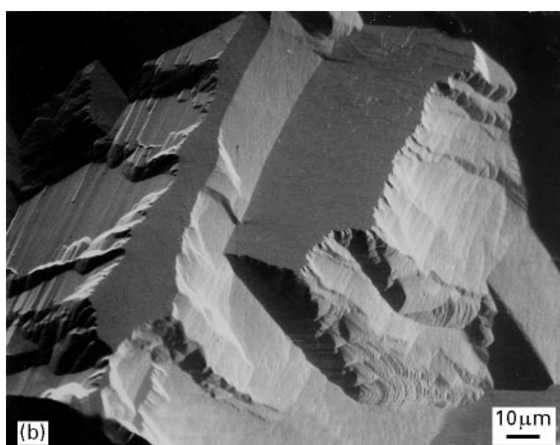

Figure 8 Terracing on sidewall of various $(h\,\bar{k}\,0)$ mesa for (a) $(3\,\bar{7}\,0)$ and (b) $(2\,\bar{3}\,0)$ plates.

Another hypothesis is that the dissolution slowness is shaped in such a manner that the $\{1\,1\,0\}$ and LP1 planes are correlated to maxima in some polar diagrams of L and to minima in other polar graphs. In this hypothesis the dominant role behaviour remains difficult to predict. Nevertheless there are no doubts about the role played by the $\{1\,1\,1\}$ plane, which etches very slowly, on the convex undercutting.

It is clear that we have to identify the final plane LP1. For this purpose let us consider the top view of an etched mesa. For $(0\,\bar{1}\,0)$ and $(1\,\bar{1}\,0)$ planes (Fig. 5(a and f)) the etched mesa intersects the masked surface along lines. For angles of cut, φ_0, ranging from 10 to 34° we observe (Fig. 5(b–e)) that the top view is also composed of linear segments even if some short portions appear to be slightly curved especially for φ_0 values closed to 23° (Fig. 5d). The angles A to E made by two successive intersecting lines and defined by the top view of Fig. 9 can be measured with an accuracy of $\pm 2°$ in the various SEM micrographs. Hence data other than those associated with somewhat curved segments are reported in Table III.

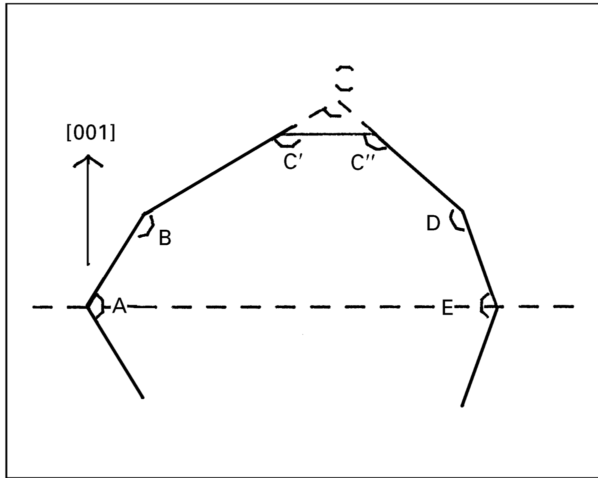

Figure 9 Definition of angles A to E associated with the intersecting linear segments which compose the top contour of $(h\,\bar{k}\,0)$ mesa.

TABLE III Experimental values for the angles A to E as defined in Fig. 9. Omitted values correspond to undistinguishable intersections

Cuts	A (deg)	B (deg)	C (deg)	D (deg)	E (deg)
$0\bar{1}0$	128	128	128	128	128
$1\bar{6}0$	150	125	155	119	155
$1\bar{4}0$	150	121	160	116	155
$3\bar{7}0$	≈ 154	≈ 144	–	–	156
$2\bar{3}0$	≈ 160	≈ 135	–	128	165
$1\bar{1}0$	159	123	126	123	159

Let β be the angle between a reference surface $(h\,\bar{k}\,0)$ and a limiting facet and let us assume that some preferential $\{h\,h\,l\}$ planes with low Miller indices which cut the top surface constitute the contour shape of the etched mesa. It becomes possible to derive theoretical values for the angle β and for angles, δ_{Mi}, in order to recognize a number of limiting facets. Thus in addition some theoretical values related to the $\{h\,h\,l\}$ and $\{1\,1\,1\}$ planes with h and l lower than five are given in Table IV. Conclusions will be drawn in section 3. At this point it is sufficient to outline a consequent terracing by planes $\{1\,1\,0\}$, $\{1\,1\,1\}$ and a plane $\{h\,h\,l\}$.

3. Theoretical 3D shapes

3.1. The 3D simulation

The simulation flow chart which is similar to that presented in our previous papers [26, 27] can be decomposed into four main stages.

(1) In the first stage we start with a mask of a given initial shape and we calculate the orientation (φ_0, θ_0, ψ, γ) of all surface elements potentially present under the mask. In the 3D simulation the orientation is defined by means of two supplementary angles (ψ, γ) with respect to the rotated reference surface with angles of cut (φ_0, θ_0) .

(2) In step two we determine the displacement, P, of all moving surface elements.

(3) Elements which disappear with prolonged etching are eliminated in the third stage using specific test procedures. At this point two important points can be made. For a membrane-like structure no problem can arise because the final etching shape depends only on the number and on the sharpness of maxima in the dissolution slowness L involved in the simulation. In the case of a mesa-like structure the top view and a cross-sectional profile at the mask edge appear to be composed of a succession of "convex" and "concave" intersections respectively. Consequently the minima

TABLE IV Calculated values (in degrees) for the inclination angle β and for the alignment angle δ related to various intersecting $\{1\,1\,l\}$ and $\{l\,l\,1\}$ planes

Cut	$(1\bar{4}0)$				$(3\bar{7}0)$				$(2\bar{3}0)$			
Facets	$l = 2$		$l = 4$		$l = 2$		$l = 4$		$l = 2$		$l = 4$	
	β	δ	β	δ	β	δ	β	δ	β	δ	β	δ
$(1\,1\,l)$	107.3	31.2	99.9	16.9	102.4	33.3	97.1	18.2	95.1	34.7	93.7	19.1
$(l\,1\,1)$	101.4	65.4	90	76.4	93.1	65.9	81.8	76.2	83.5	65.7	70.9	75.6
$(\bar{1}\,1\,l)$	119.7	20	106.6	10.3	122.4	14.7	108.0	7.5	124.5	7.9	109.1	4.0
$(\bar{l}\,1\,1)$	126.4	59.5	117.2	74.6	134.2	55.3	126	73.1	142.4	48.0	136.0	70.2
$(l\,l\,1)$	119	67.6	120.4	78.4	110.5	69.2	111.5	79.2	100.6	70.2	101.1	79.8
$(1\,l\,l)$	124.5	36	129.3	25.9	118.8	40.5	124.9	32	111.7	44.1	118.9	37.3
$(\bar{1}\,l\,l)$	136.7	13.6	135.9	14.0	138.1	3.8	135.1	9.3	137.5	7.9	109.1	4.0
$(\bar{l}\,l\,1)$	143	55.5	147.6	71	151.1	46.4	156.1	64.5	157.6	29.0	164.9	48

and maxima in L interact to determine the final etching shape which in reality results from a competition between extrema of different nature. To derive numerically the etching shape of the mesa we have decided that maxima in L play the most important role and limit a first the etched structure.

(4) Two different types of graphical representations are proposed in the final stage. A constant-level contour diagram which allows us to appreciate the degree of anisotropy of the chemical attack. This diagram also has the advantage of calling attention to regions where limiting planar facets, curved sidewalls or edges with sharp reflex angles develop. Secondly, the lateral underetch, U_L, under the mask, the inclination of a limiting facet or the extent of a curved region can be determined using dissolution profiles corresponding to various cross-sectional plane, $\mathfrak{P}_i$, intersecting the reference surface along lines L_i.

The major problem which arises in the 3D simulation concerns the number of data involved in the test procedures of stage 3. To reduce the size of matrices which appears to be critical, increments in the angles ψ and γ have been increased to 1° and 2° respectively. Adopting these increments the total running time reaches nevertheless 4 h.

This 3D numerical and graphical simulation was used to derive theoretical dissolution shapes for membrane- and mesa-like structures in the special case where we start with an inert mask of circular shape. Thus we can undertake systematic comparisons of experimental and theoretical shapes in order firstly to be more precise about the real respective contribution of maxima and minima in L to the formation of etched structures and secondly, to estimate the adequation of the proposed dissolution slowness surface is satisfactory.

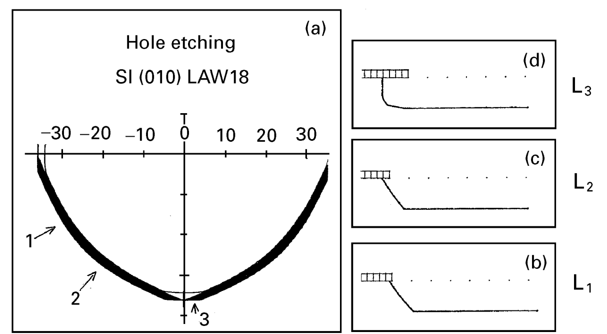

Figure 10 Theoretical etching shapes for a $(0\bar{1}0)$ membrane; (a) constant-level contours diagram; (b, c, d) cross-sectional dissolution profiles related to intersecting lines L_1, L_2 and L_3 respectively (as indicated by arrows in (a)).

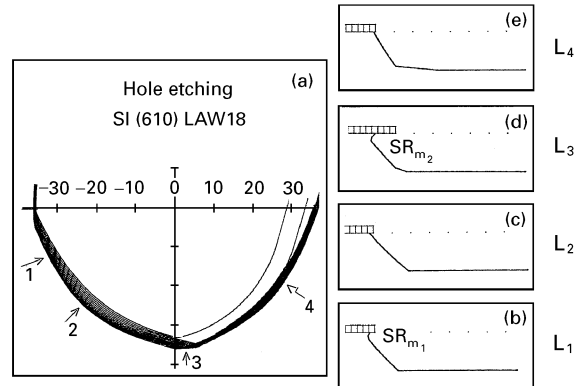

Figure 11 Theoretical etching shapes for a $(1\bar{6}0)$ membrane; (a) *constant-level contours diagram*; (b, c, d, e) cross-sectional dissolution profiles related to intersecting lines L_1, L_2, L_3 and L_4 respectively (as indicated by arrows in (a)).

3.2. Theoretical etching shapes for membranes

Starting with the dissolution slowness surface presented in part I and II of this work [31, 32] and with the $(0\bar{1}0)$, $(1\bar{6}0)$, $(3\bar{7}0)$ and $(2\bar{3}0)$ reference surfaces we obtain the theoretical representations for etched membranes displayed in Figs 10(a–d)–13(a–e). Some characteristic cross-sectional profiles are also selected.

Let us recall that for singly-rotated $(h\bar{k}0)$ planes the rotated x'_1 axis, which in the constant level contour diagrams corresponds to the horizontal axis, lies in the cross-sectional plane (001). Thus since this plane acts as a mirror plane it is sufficient to give a half theoretical shape with respect to the x'_1 axis. In this condition the running time of the simulation is divided by two. Moreover all the graphical representations presented in this section are derived with the same duration of etching in order to give the comparison with experiments more significance.

The simulation applied to a $(0\bar{1}0)$ membrane leads to the development of planar facets (planes P_{m1}) easily depicted in Fig. 10(a–d) whose inclination corresponds to that of $\{111\}$ planes. Clearly the top contour formed by these bordering planes remains more curved than in the SEM of Fig. 2a. As care has been taken that the theoretical ratio of the initial diameter of the circular mask on the etch depth does not differ very much from the experimental ratio this departure can be partly attributed to a deviation in the dissolution slowness ratio $L\{111\}/L\{100\}$. However the simulation indicates (Fig. 10(a and d) that the bordering (100) and (001) planes intersect the reference surface along straight line segments in accord with experiment.

Figs 11a–13a and 14a show evidence of a progressive destruction of the four-fold symmetry of the (010) membrane as we rotate the $(0\bar{1}0)$ plane about the x_3 axis (the crystallographic [001] direction). From a general point of view the experimental evolution of etching shapes for membranes as illustrated in Fig. 2(a–d) appears to be satisfactorily fitted by the theoretical diagrams of Figs 10(a–d)–13(a–e). Several interesting points emerge from these figures.

(i) As the angle of cut φ increases from 0 to 45° the numerical simulation produces three limiting $\{111\}$ facets (Planes P_{m1}, P'_{m1} and P''_{m1}). It is clear that plane P''_{m1} becomes increasingly more vertical whereas the other facet P'_{m1} becomes continuously less inclined with respect to the reference surface which is in agreement with the experimental observations.

Moreover the third facet P_{m1} contributes to the formation of a sharp edge SR_{m1} (see for example Figs 11b and 12b) with the facet P'_{m1}. The second "sharp"

region SR_{m2} is partly correlated with the intersection of facets P'_{m1} and P''_{m1} (Figs 11e, 12d and 13d for example).

(ii) Two other limiting facets (denoted P_{m2} and P'_{m2}) participate in the final etching shape. In particular facet P'_{m2} (Fig. 12a) intersects the limiting {1 1 1} facet P''_{m1} in close proximity to the sharp edge SR_{m2}. This sharp region corresponds approximately to a cross-sectional intersecting line with an alignment angle of about $270° + \varphi_0$ as illustrated by the cross-sectional profiles of Figs 11d and 12d.

(iii) It is clear from the simulation that sharp edges SR_{m1} and SR_{m2} disappear as the angle of cut reaches 45° because facets P_{m1} and P''_{m1} become progressively vertical (compare for example the dissolution profiles displayed in Figs 12b, 13b and 14b). Consequently we can convincingly state that facets P_{m1} and P''_{m1} are {1 1 1} limiting facets.

(iv) As suggested in note (ii) the constant-level contour diagrams of Figs 11a–14a reveal that (0 1 0) and (1 0 0) planes also bound etched membranes. A previous paper [37] indicated that secondary maxima in the dissolution slowness occur for {1 0 0} orientations. Consequently depending on the respective amplitude of the {1 0 0} and {1 1 1} maxima and on the initial diameter of the inert mask, facets P_{m2} and P'_{m2} can effectively contribute to the final structure. Since these facets form with the reference an $(h\bar{k}0)$ surface at an angle equal to the angle of cut φ_0 (facet P'_{m2}) it is easy for the reader to verify that changes in the inclinations depicted on the theoretical diagrams follow this evolution.

In theory a perfectly planar facet P_{mi} with an inclination angle, β_{mi}, with respect to the reference surface intersects the etched surface along a line L_{mi} which makes an alignment angle δ_{mi} with the rotated axis (see for example Fig. 13a). Hence it may be of interest to compare calculated, theoretical and experimental values for the angles δ_{mi} and β_{mi} (Tables V and VI). Tables V and VI have been compiled assuming that the sidewalls are essentially composed of {1 1 1} and {1 0 0} facets. Moreover to estimate the δ_{mi} angles for the various {1 1 1} facets we have assumed that for each cross-sectional profile the intersecting line L_{mi} is tangential to the part of the deeper contour which is nearest to the initial centre of the membrane. The direction of alignment of facet P_{m1} remains difficult to estimate. However evaluation is easier for facets P'_{m1} and P''_{m1} for which deviations less than 2° are obtained (Table V). Moreover a rapid comparison of values for the inclination angle as displayed in Table VI with the cross-sectional profiles of Figs 10(a–d)–14(a–c) shows a qualitative agreement for all the theoretical $(h\bar{k}0)$ membranes illustrated in Figs 10(a–d)–14(a–c).

A final remark to underline the very small lateral underetch that all the cross-sectional dissolution profiles (Figs 10(a–d)–14(a–c)) exhibit under the mask. This behaviour is understood in terms of limiting {1 1 1} facets which dissolve very slowly and

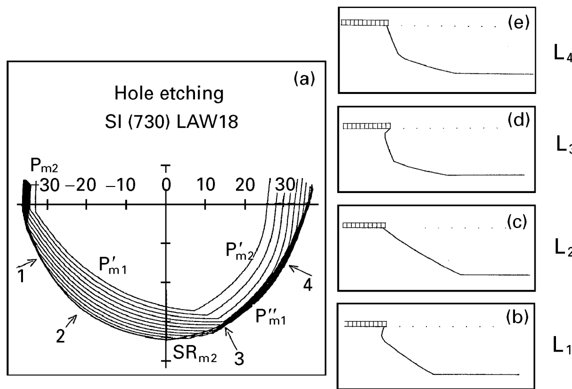

Figure 12 Theoretical etching shapes for a $(3\bar{7}0)$ membrane; (a) constant-level contours diagram; (b, c, d, e) cross-sectional dissolution profiles related to intersecting lines L_1, L_2, L_3 and L_4 respectively (as indicated by arrows in (a)).

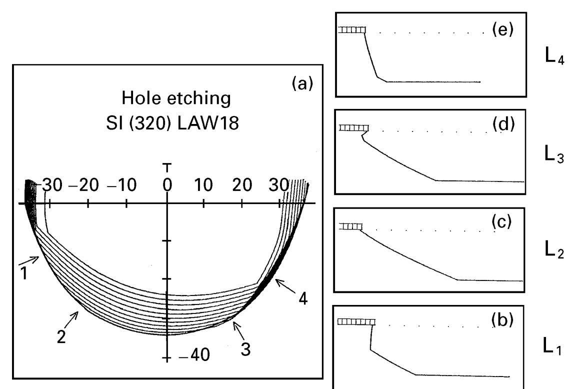

Figure 13 Theoretical etching shapes for a $(2\bar{3}0)$ membrane; (a) constant-level contours diagram; (b, c, d, e) cross-sectional dissolution profiles related to intersecting lines L_1, L_2, L_3 and L_4 respectively (as indicated by arrows in (a)).

TABLE V Calculated, numerical (simulation) and experimental values of the alignment angle δ_{mi} related to various limiting LP2 ({111} planes) facets. Numerical and experimental values are estimated (from contour diagrams and SEM micrographs respectively with an accuracy of $\pm 2°$. Omitted values are for undistinguishable intersecting lines L_{mi}. Limiting facets P_{m1}, P'_{m1} and P''_{m1} correspond to $(11\bar{1})$, $(1\bar{1}\bar{1})$ and $(\bar{1}\bar{1}\bar{1})$ planes respectively

	Calculated values (deg)			Numerical values (deg)			Experimental values (deg)		
Planes	P_{m1}	P'_{m1}	P''_{m1}	P_{m1}	P'_{m1}	P''_{m1}	P_{m1}	P'_{m1}	P''_{m1}
$(1\bar{6}0)$	131	140.6	49	–	138	48	–	141	49
$(3\bar{7}0)$	127.3	152.3	52.7	124	154	53	–	154	53
$(2\bar{3}0)$	125.8	164.5	54.2	126	163	55	–	164	55
$(1\bar{1}0)$	125.3	180	54.7	123	180	57	–	–	–

TABLE VI Calculated values of the inclination angle β_{mi} that a limiting facet P_{mi} forms with the reference surface. Note that P_{m2} and P'_{m2} facets correspond to the LP3 facets (section 2)

Planes	$P_{m1}:(11\bar{1})$	$P'_{m1}:(1\bar{1}\bar{1})$	$P''_{m1}:(\bar{1}\bar{1}\bar{1})$	$P_{m2}:(100)$	$P'_{m2}:(010)$
$(0\bar{1}0)$	125.3	54.7	54.7	90	0
$(1\bar{6}0)$	118.3	48.4	61.6	99.5	9.5
$(3\bar{7}0)$	107.6	40.7	72.3	113.2	23.2
$(2\bar{3}0)$	99.2	36.8	80.7	127.3	37.3
$(1\bar{1}0)$	90	35.3	90	135	45

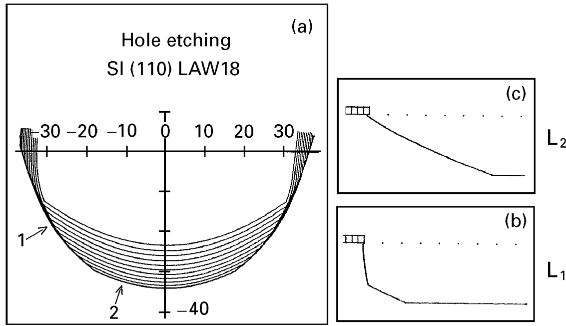

Figure 14 Theoretical etching shapes for a $(1\bar{1}0)$ membrane; (a) constant-level contours diagram; (b, c) cross-sectional dissolution profiles related to intersecting lines L_1 and L_2 respectively (as indicated by arrows in (a)).

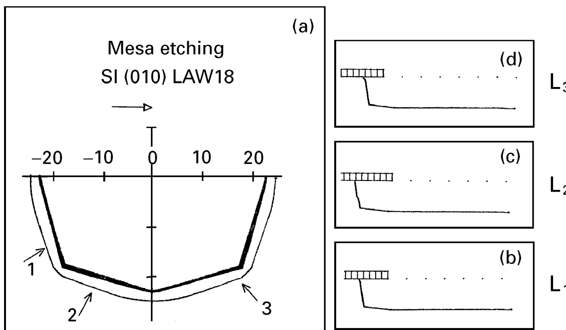

Figure 15 Theoretical etching shapes for a $(0\bar{1}0)$ mesa; (a) constant-level contours diagram; (b, c, d) cross-sectional dissolution profiles related to intersecting lines L_1, L_2 and L_3 respectively (as indicated by arrows in (a)).

consequently edge the major part of the membranes. In connection with this remark it is left to the reader to verify that values of δ_{mi} collected in Table V and related to $\{1\,1\,1\}$ facets are close to the values evaluated from SEM images of pin-holes (Table II).

In conclusion, for etched membranes the 3D simulation gives evidence for the important role played by maxima maximora in relation to $\{1\,1\,1\}$ facets and also the contribution of $\{1\,0\,0\}$ facets to the final etching shape. The 3D simulation and especially the cross-sectional dissolution profiles greatly facilitate the identification of limiting planar facets or curved regions which constitute the bordering edges of micromachined membranes and which find their origin in the proximity of maxima for L.

3.3. Theoretical etching shapes for mesa

The theoretical shapes of various $(h\,\bar{k}\,0)$ mesa (Figs 15a–20a) as derived from the graphical simulation look like the experimental shapes. At first sight the agreement concerns primarily the following features:

(i) The contour shape cut in the upper surface which is generally caused by convex undercutting [13, 14, 39]. We note the fact that depending on the face that has been masked it may be necessary to rotate the etched mesa by 180° about the normal to the $(h\,\bar{k}\,0)$ plate to find the graphical diagram again. This is in particular the case for mesa structures micro-machined in $(3\,\bar{7}\,0)$ and $(2\,\bar{3}\,0)$ planes (Figs 18(a–e) and 19(a–e)).

(ii) The formation on $(1\,\bar{6}\,0)$ and $(1\,\bar{4}\,0)$ mesa of a somewhat curved and slightly disorientated facet SH_2 (Figs 6e, and 17(a and e)) which joints a nearly vertical plane P_{M4} to the etched reference surface. As the angle of cut φ_0 increases from 23 to 45° this curved shoulder becomes continuously more sloping. This evolution (Fig. 5(a–f)) is conveniently illustrated by the constant-level contour diagrams displayed in Figs 16a–20a and by the cross-sectional profiles of Figs 16e–19e.

(iii) The development of a sharp region SR (see for example Fig. 18a related to a $(3\,\bar{7}\,0)$ mesa) which penetrates to varying extents under the mask and whose acute angle results from the intersection of an inward and a subsequent outward "facet" (Figs 18d and 19d). The depth of penetration seems more significant for angles of cut in the vicinity of 30° (Figs 18a and 19a). Moreover this sharp region disappears in theory for $(0\,1\,0)$ and $(1\,\bar{1}\,0)$ mesa (Figs 15a and 20a). Rapid examination of SEM micrographs (Fig. 5(a–f)) shows that the experimental shapes crudely follow this behaviour.

(iv) The presence (Figs 16a–20a) of a special bevel (denoted SB on diagrams) for cuts with angle φ_0 ranging from 10–45°. Comparison of theoretical and experimental shapes indicates that this bevel is generated in a region which in the experimental mesa is characterized by the formation of terraces (Figs 5(a–f) and 8(a and b)). Moreover the spread of this bevel increases with the angle of cut in close agreement with experimental observation.

Owing to the general agreement between experimental and theoretical shapes related to $(h\,\bar{k}\,0)$ mesa it may be of interest to extend the comparison. For this purpose let δ_{Mi} be the angle that the successive linear segments, LS_i which constitute the top contour shape of mesa, make with the horizontal x'_1 axis (Fig. 17a).

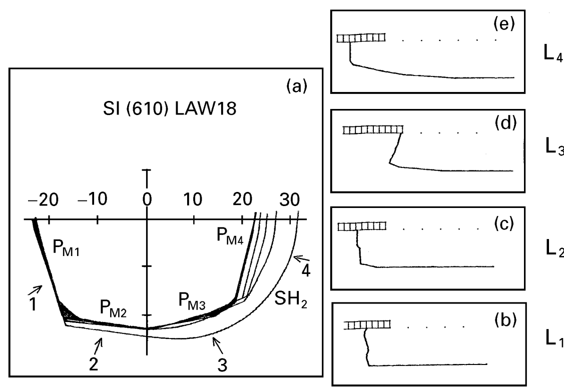

Figure 16 Theoretical etching shapes for a $(1\,\bar{6}\,0)$ mesa; (a) constant-level contours diagram; (b, c, d, e) cross-sectional dissolution profiles related to intersecting lines L_1, L_2, L_3 and L_4 respectively (as indicated by arrows in (a)).

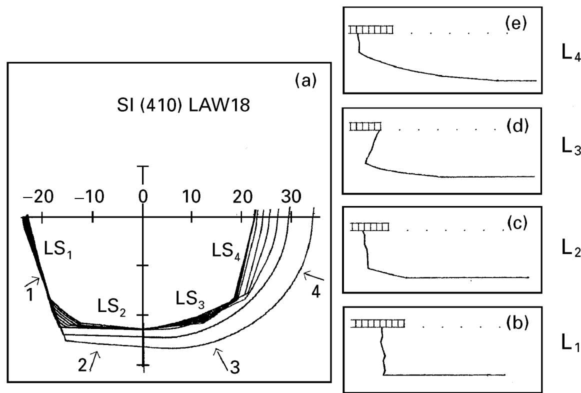

Figure 17 Theoretical etching shapes for a $(1\,\bar{4}\,0)$ mesa; (a) constant-level contours diagram; (b, c, d, e) cross-sectional dissolution profiles related to intersecting lines L_1, L_2, L_3 and L_4 respectively (as indicated by arrows in (a)).

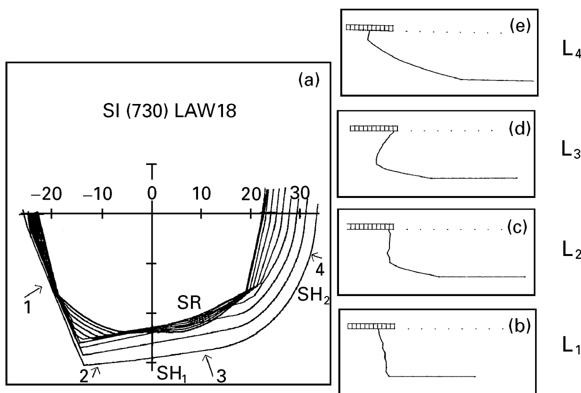

Figure 18 Theoretical etching shapes for a $(3\,\bar{7}\,0)$ mesa; (a) constant-level contours diagram; (b, c, d, e) cross-sectional dissolution profiles related to intersecting lines L_1, L_2, L_3 and L_4 respectively (as indicated by arrows in (a)).

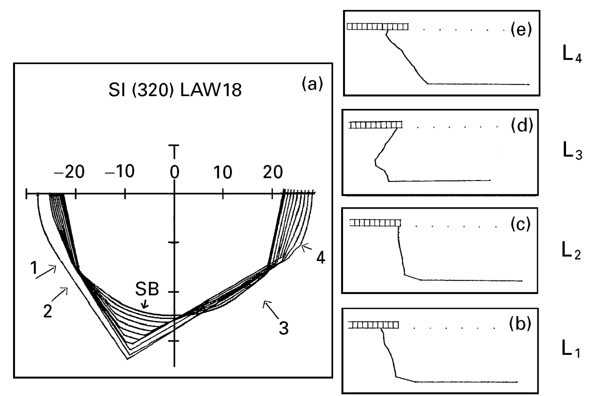

Figure 19 Theoretical etching shapes for a $(2\,\bar{3}\,0)$ mesa; (a) constant-level contours diagram; (b, c, d, e) cross-sectional dissolution profiles related to intersecting lines L_1, L_2, L_3 and L_4 respectively (as indicated by arrows in (a)).

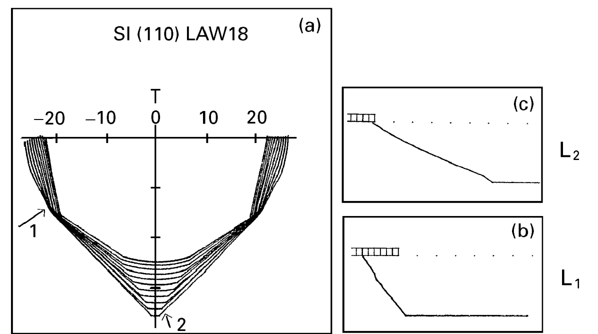

Figure 20 Theoretical etching shapes for a $(1\,\bar{1}\,0)$ mesa; (a) constant-level contours diagram; (b, c) cross-sectional dissolution profiles related to intersecting lines L_1 and L_2 (as indicated by arrows in (a)).

Experimental values and theoretical values extracted from the simulation are reported in Table VII. Note that we have assumed that the direction for the horizontal axis is that indicated by the arrow in Fig. 15a. For angles of cut smaller than 23° four linear segments can be distinguished both on contour diagrams (Figs 15a–17a) and on SEM micrographs (Fig. 5(a–f)). The third segment LS_3 is associated with the inward facet LP_3 of region SR. Furthermore the angle δ_{M2} related to the second segment LS_2 under which the terraced region develops remains difficult to evaluate on theoretical $(3\,\bar{7}\,0)$ and $(2\,\bar{3}\,0)$ mesa. Nevertheless the agreement between theoretical and experimental values seems very satisfactory. In this condition attempts can be made to recognize facets limiting the etched structure.

At this point let us recall that in the literature [11, 13, 14, 39] different beveling faceting planes have been proposed. Depending on the etchant $\{2\,1\,1\}$ [11], $\{2\,1\,1\}$ [14], $\{3\,3\,1\}$ [11, 34] and $\{4\,1\,1\}$ [13] planes have been identified. In particular for aqueous KOH solutions the role played by the $\{4\,1\,1\}$ and $\{3\,3\,1\}$ planes in the underetching of convex corners has been highlighted. Taking into account the diversity of results reported in the literature, tentative arguments are proposed to explain the convex undercutting observed in experimental shapes in terms of limiting $\{h\,h\,l\}$ facets.

With this aim, consider the $(0\,1\,0)$ mesa (Fig. 5a) which clearly shows an octagonal convex corner

TABLE VII Values for the angle δ_{Mi} as estimated from constant-level contour diagrams and from SEM micrographs of the mesa. The evaluation is made at roughly two degrees. The superscript[a] indicates an average value determined when segment 3 is composed of two slightly disorientated linear segments S_{Mi} or a value corresponding to an inward facet intersecting the consecutive outward facet rather than intersecting the masked surface

Reference surface	Degree	Segment 1 δ_{M1} (deg) Theory	Experiment	Segment 2 δ_{M2} (deg) Theory	Experiment	Segment 3 δ_{M3} (deg) Theory	Experiment	Segment 4 δ_{M4} (deg) Theory	Experiment
$(0\,1\,0)$	0	105	106	165	164	15	16	75	74
$(1\,\bar{6}\,0)$	9.5	104	104	171	169	13	15	76[a]	76[a]
$(1\,\bar{4}\,0)$	14	105	105	174	170	18[a]	18[a]	76	76
$(3\,\bar{7}\,0)$	23.2	103	102	≈ 143	145	21[a]	22[a]	78	77
$(2\,\bar{3}\,0)$	33.7	100	98	≈ 143	145	28[a]	28[a]	80	82
$(1\,\bar{1}\,0)$	45	100	100	140	142	30	28	80	80

undercutting. Since the angle δ_{Mi} measured from the SEM micrograph are close to $16°, 90° \pm 16°$ and $180° - 16°$, the intersecting lines lie parallel to $\langle 3\,1\,0\rangle$ directions. Because of this observation we have only to deal with bevel planes such as the $\{3\,1\,1\}$ and $\{3\,3\,1\}$ planes. As an example in Fig. 21a are drawn the limiting $\{3\,1\,1\}$ facets which *a priori* surround a $(h\,\bar{k}\,0)$ mesa. It is clear that the segment LS_2 is associated with the intersecting plane $(1\,1\,3)$. Facets $(\bar{1}\,1\,3)$ and $(\bar{1}\,\bar{1}\,3)$ give rise to a sharp dissolution profile (Fig. 21b) so that we can estimate that the angle δ_{M3} related to segment LS_3 is primarily determined by the inward facet $(\bar{1}\,\bar{1}\,3)$ for most of the cuts investigated here.

The facet $(3\,\bar{1}\,1)$ is certainly correlated with segment LS_1 whereas the intersection of inward $(\bar{3}\,\bar{1}\,1)$ and outward $(\bar{3}\,1\,1)$ facets (Fig. 21c) occurs in the vicinity of segment LS_4. We can now undertake a comparison of values for the angle δ_{Mi} as calculated from simple geometrical considerations (Table VIII) with experimental values (Table VII).

It is evident that as soon as φ_0 reaches 19° the intersecting segment LS_3 results principally from the formation of the inward $(\bar{1}\,\bar{1}\,3)$ facet. If we turn our attention to the changes in the angles δ_{M2} and δ_{M3} with the cut $(h\,\bar{k}\,0)$ we observe that the general behaviour depicted in Table VIII agrees crudely with experiments and with the evolution derived from simulation (Table VII). Less satisfactory are the calculated changes in the angle δ_{M4} (or δ_{M1}) related to segment LS_4 (or LS_1). Effectively Table VIII reveals a small but continuous decrease (or increase) in δ_{Mi} with increasing values for the angle of cut, φ_0. This evolution doesn't illustrate the experimental and theoretical changes presented in Table VII. In reality only intersecting lines related to $(h\,h\,1)$ faces with a Miller index h greater than 2 can account for the observed continuous increase in δ_{M4}. Consequently it is of interest to investigate the possibility of a convex corner undercutting partly governed by $\{3\,3\,1\}$ facets. For this purpose we have also reported in Table VIII values of the angles δ_{Mi} formed by $\{3\,3\,1\}$ limiting planes. It is left to the reader to show that in this case convex corners are undercut by a set of $\{3\,3\,1\}$ facets in such a way that this set may be easily deduced from the preceding $\{3\,1\,1\}$ set by replacing the second Miller index 1 or $\bar{1}$ by 3 or $\bar{3}$. The variations in the angle δ_{Mi} with the cut now do not depart very much from

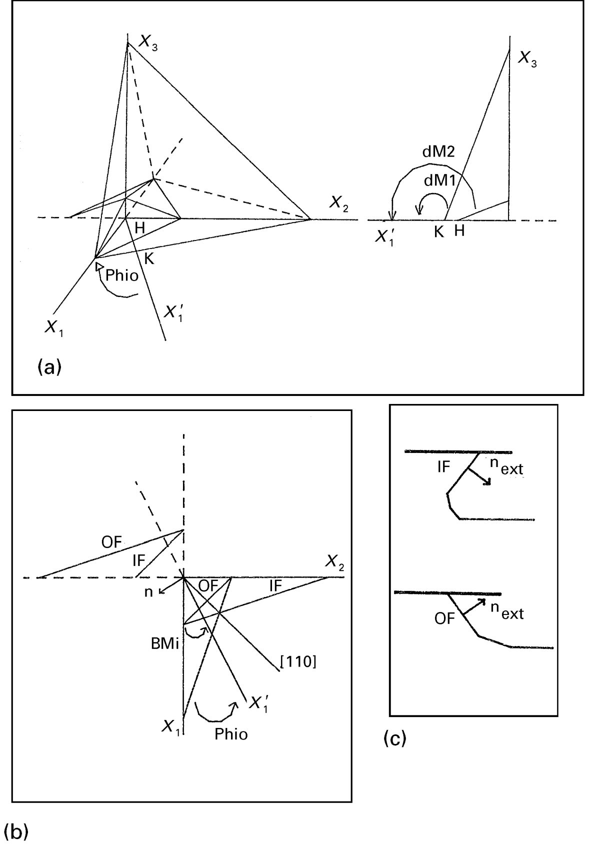

Figure 21 (a) Some $\{1\,1\,3\}$ facets which can surround the $(h\,k\,0)$ mesa and correspond to an alignment angle δ_{Mi} inclination; (b) definition of alignment angle βM_i related to the intersecting line Ox'_1 and (c) definition of inward (IF) and outward (OF) facets.

the experimental and numerical ones specially for φ_0 values greater than 19°. This result suggests that $\{3\,3\,1\}$ facets may be involved in the convex corner undercutting. To continue with this assumption we have to evaluate the inclination angles β_{M1} and β_{M4} that the limiting facets in question form in the cross-sectional plane $(0\,0\,1)$ (i.e., for a dissolution profile corresponding to rotated axis x'_1, Fig. 21b). For the outward $(3\,3\,1)$ facet Table IX indicates that the apparent inclination angle varies from 45° (for $(0\,\bar{1}\,0)$ mesa) to 90° (for $(1\,\bar{1}\,0)$ mesa). Moreover for the same intersecting line x'_1 the $(3\,1\,1)$ facet acts as an inward facet for cuts with $\varphi_0 > 19°$ and as an outward facet for cuts

TABLE VIII Calculated values for angles δ_{Mi} related to segments LS_i assuming that mesa are only bounded by either {3 1 1} facets or {3 3 1} facets. Values with the superscript "a" correspond to an inward facet forming a sharp edge with subsequent surface element

Cuts $(h\bar{k}0)$	δ_{M1} (deg)		δ_{M2} (deg)		δ_{M3} (deg)		δ_{M4} (deg)	
	{311}	{331}	{113}	{133}	{113}	{133}	{311}	{331}
$(0\bar{1}0)$	108.4	108.4	161.6	161.6	18.4	18.4	71.6	71.6
$(1\bar{6}0)$	102.2[a]	106.2[a]	159	170.7	15	9.3	72.2[a]	73.8[a]
$(1\bar{4}0)$	107.6	105.4	158	175.4	22[a]	29.5[a]	72.4	74.6
$(3\bar{7}0)$	107.6	104.2	156.3	175	23.7[a]	35[a]	72.4	75.8
$(2\bar{3}0)$	108.2	103.5	155.2	164.5	24.8[a]	39.7[a]	71.8	76.5
$(1\bar{1}0)$	109.5	103.3	154	154.8	25.3	25.3	70.5	76.7

TABLE IX Calculated values for the apparent inclination angle, β^a_{Mi}, for facets {3 3 1} and {3 1 1} associated with intersecting segments LS_1 and LS_4. Values greater than 90° indicate that the dissolution profile lying in the cross-sectional (0 0 1) plane is composed under the mask by an inward facet

Cuts	$0\bar{1}0$	$1\bar{6}0$	$1\bar{4}0$	$3\bar{7}0$	$2\bar{3}0$	$1\bar{1}0$
			facets {3 3 1}			
$\beta^{a'}_{M1}$ (deg)	45	54.5	59	68.2	78.7	90
$\beta^{a'}_{M4}$ (deg)	135	125.5	121	111.8	101.3	90
			facets {1 1 3}			
β^{a}_{M1} (deg)	71.6	81.1	85.6	94.8	105.3	116.6
β^{a}_{M4} (deg)	108.4	98.9	94.4	85.2	74.7	63.4

TABLE X Apparent inclination of the (1 3 1) facet with respect to the reference plane $(h\bar{k}0)$

Cuts	$(0\bar{1}0)$	$(1\bar{6}0)$	$(1\bar{4}0)$	$(3\bar{7}0)$	$(2\bar{3}0)$	$(1\bar{1}0)$
$\beta^a_{(131)}$ (deg)	18.4	27.9	32.5	41.6	52.1	63.4

close to the (0 1 0) plane ($\varphi_0 < 18°.5$). In view of the SEM micrographs displayed in Fig. 5(d and e) in which facets appear to be too white it is difficult to decide if, for cuts with $\varphi_0 > 19°$, the convex corner undercutting is due to an inward (3 1 1) facet or to a nearly vertical (3 3 1) facet. In those conditions a decision based on the changes in the angles δ_{M1} and δ_{M4} remains attractive and we cannot rule out the possibility that {3 3 1} facets participate in undercutting the segment lines LS_1 and LS_4 especially in the case where φ_0 has a value greater than 19°. Moreover for these cuts ($\varphi_0 > 19°$) the shoulder SH_1 (Fig. 18a) which joins the unmasked surfaces may perhaps be composed of surface elements close to the (1 3 1) plane. Effectively the changes in the inclination $\beta^a_{(131)}$ (Table X) reflect variations in the lateral extent of this shoulder with the angle of cut (Fig. 5(d and e) as well as Figs 18a and 19a) even if the inclinations seem too accentuated for cuts with φ_0 close to 19°.

Let us also recall that the magnified SEM image of Fig. 7 shows a texture which is quite similar to those which develop on {1 1 3} and {1 1 4} etched plates [13, 40]. The hypothesis that for cross-sectional directions in the vicinity of the rotated axis x'_1 (3 3 1) and (1 3 1) facets can compose the cross-sectional dissolution profile is also sustained by the fact that these facets possess a common [0 3 1] direction.

For $(1\bar{6}0)$ and $(1\bar{4}0)$ mesa the rather curved shoulder SH_2 (here at the right of the SEM image) results from the successive intersections of surface elements slightly disoriented with respect to the reference surface. Effectively Fig. 6 reveals the formation of a large concave background on the shoulder which is quite identical to the texture which develops on etched (0 1 0) plates. In the same way changes in the average inclination of the curved shoulder SH_2 as given by the theoretical cross-sectional profiles of Figs 16e and 17e support this explanation.

4. Discussion and conclusion

We will discuss the formation of limiting planar facets or curved regions in terms of maxima and minima in the dissolution slowness surface as presented in our previous papers [31, 32]. First of all a close resemblance between the experimental and theoretical shapes for membranes is observed for all the $(h\bar{k}0)$ cuts investigated in the present work. This agreement

is not surprising since the proposed dissolution slowness surface exhibits only three basic maxima in L for $\{1\,0\,0\}$, $\{1\,1\,0\}$ and $\{1\,1\,1\}$ planes and only maxima determine the final etching shape of a starting completely concave structure [10, 22, 24, 38, 41, 42]. The case of mesa-like structures is more complicated and calls for several comments. For the first time emphasis can be placed on the convex corner undercutting which concerns the $(1\,\bar{1}\,0)$ mesa. Several authors [38, 39, 43] have argued that this undercutting is intimately connected with the presence of minima in the dissolution slowness. If we retain this argument for a $(1\,\bar{1}\,0)$ we have to look to the two minima minimora that the polar plot of L only exhibits in a $\{1\,1\,0\}$ section (x'_1, x_3) section. Let us recall that these minima occur for directions obtained by rotations of about 9 and 63° about the x'_2 axis [31, 32]. Thus these directions lie crudely parallel to the $\langle 4\,4\,1\rangle$ and $\langle 1\,1\,3\rangle$ crystallographic directions as shown in Table XI which gives values for the angle of rotation related to various $(h\,h\,l)$ planes. The fact that the proposed dissolution slowness surface generates minima for surface elements in the close vicinity of $\{1\,1\,3\}$ planes contributes to the agreement between the theoretical and experimental general shapes of $(h\,\bar{k}\,0)$ mesa.

In addition the probable participation of $\{4\,1\,1\}$ facets in the theoretical contour shape of $(3\,\bar{7}\,0)$ and $(3\,\bar{2}\,0)$ mesa intensifies the impression of satisfactory accord between theory and experiments. Effectively deviations between calculated values for the angles δ_{M1} and δ_{M4} and for inclination angles related to $\{3\,3\,1\}$ and $\{4\,1\,1\}$ facets do not exceed 3° (Tables VIII, IX and XII) if the angle of cut, φ_0, is greater than 19°.

Another important feature which emerges from the study of mesa-like structures is that far from the mask edge the formation of a curved shoulder sems to be correlated to maxima in the dissolution slowness L. Thus we can infer that in the furthermost regions a competition between less pronounced minima and maxima takes place. Consequently in the absence of graphical and numerical simulation procedures the prediction of resulting shapes for such shoulders is both risky and tentative.

A general agreement between the theoretical and experimental etching shapes follows from this work and we can try to advance the investigation by a discussion of the relative amplitude for the successive extrema in L. For this purpose we undertake a crude comparison between the experimental and theoretical extents of some planar and curved facets bounding membranes and then follow the evolution of the theoretical and experimental width of shoulders related to mesa. Tables XIII and XIV summarize the situation for $(h\,\bar{k}\,0)$ membranes. We obtain deviations less than 20% for the reduced ratio of facet extent especially in the case of P_{m2} and P'_{m2} facets. Since for these facets the evolution illustrated by Table XIII also reflects the changes in the etch rate for $(h\,\bar{k}\,0)$ plates this result can

TABLE XI Values for the angle ψ that $[h\,h\,l]$ directions make with the rotated axis $[1\,7\,0]$

Direction $[h\,h\,l]$	[6 6 1]	[4 4 1]	[3 3 1]	[2 2 1]	[1 1 2]	[1 1 3]	[1 1 4]	[1 1 6]
Ψ (deg)	6.7	10	13.3	19.5	54.7	64.7	70.5	77

TABLE XII Calculated values for angles δ_{Mi} and inclinations of β_{Mi} related to some outward and inward (superscript[a]) limiting facets $\{4\,4\,1\}$

Cuts	Planes				Planes			
	P_{M1}		P^a_{M1}		P_{M4}		P^a_{M4}	
	β_{M1} (deg)	δ_{M1} (deg)	β^a_{M1} (deg)	δ^a_{M1} (deg)	β_{M4} (deg)	δ_{M4} (deg)	β^a_{M4} (deg)	δ^a_{M4} (deg)
$(0\,1\,0)$	45.9	104	134.1	104	45.9	86	134.1	86
$(1\,\bar{6}\,0)$	36.7	106.9	124.9	102.2	55.1	77.7	143.2	73.08
$(1\,\bar{4}\,0)$	32.4	108.9	120.4	101.6	59.6	78.4	147.6	71
$(3\,\bar{7}\,0)$	23.9	115.5	111.5	100.8	68.5	79.2	156.1	65.5
$(2\,\bar{3}\,0)$	15.1	132	101.1	100	78.9	79.8	164.9	48
$(1\,\bar{1}\,0)$	10	180	90	100	90	80	170	0

TABLE XIII Reduced ratio of the extent for P'_{m1}, P_{m2} and P'_{m2} facets with respect to $(1\,\bar{6}\,0)$ etched membranes. The error is estimated to be ± 10%

Cuts	Experimental			Theory		
	P_{m2}	P'_{m2}	P'_{m1}	P_{m2}	P'_{m2}	P'_{m1}
$(1\,\bar{6}\,0)$	1	1	1	1	1	1
$(3\,\bar{7}\,0)$	3	1.2	2	3	1.4	2.5
$(3\,\bar{2}\,0)$	4	0.7	2.5	3.5	0.6	2.8

TABLE XIV Reduced ratio of the lateral extent of shoulder $\mathbf{SH_2}$ (with respect to the shoulder formed on $(1\bar{1}0)$ mesa

Cuts	Experimental	Theory
$(1\bar{6}0)$	3.5	2.2
$(1\bar{4}0)$	3.7	2.7
$(3\bar{7}0)$	3.2	2.5
$(2\bar{3}0)$	2.2	1.5
$(1\bar{1}0)$	1	1

be understood in terms of a very satisfactory fit of the $\{100\}$ polar plot of L in accord with previous conclusion [31, 32]. More significant are the departures observed for the reduced ratio of the lateral extent of the mesa shoulder SH_2 (Table XIV). Variations in this ratio, as predicted by numerical simulation, are characterized by a maximum which occurs for φ_0 values around 14°. The experimental ratio passes through a maximum for a quite similar angle of cut. But the theoretical value departs from the experimental one: the deviation exceeds 25% for all the $(h\bar{k}0)$ mesa. Thus changes in the curvatures for the shoulder SH_2 are not perfectly reproduced by the numerical simulation. Let us recall that the lateral extent of a curved shoulder results from the degree of divergence for the displacement vector [41, 42] associated with moving the surface elements which compose the shoulder. This is equivalent to saying that this extent is determined partly by accentuation of extrema and partly by the relative amplitude of successive extrema in L.

Hence these departures indicate that even if the proposed dissolution slowness surface seems satisfactory we have to perform some additional adjustments which concern either the relative amplitude or the sharpness of some extrema, especially minima in L. This adjustment should be applied to the micromachining of new rotated silicon plates. The study of membranes and mesa etched in doubly rotated (hhl) plates is particularly convenient in view of this work. This experimental work will be reported and discussed in a future paper.

Acknowledgement
The author greatly acknowledges A. Brahim-Bounab for providing the micro-machined $(hk0)$ silicon structures.

References
1. P. L. CHEN, R. S. MULLER, R. D. JOLLY, G. L. HALAC, R. M. WHITE, A. P. ANDREWS, T. C. LIM and M. E. MOTOMEDI, *IEEE Trans. Electron Devices* **29** (1982) 27.
2. K. E. PETERSEN, A. SHARTEL and N. F. RALEY, *ibid.* **29** (1982) 23.
3. G. S. SANDER, J. W. KNUTTI and J. D. MEINDL, *ibid.* **27** (1980) 927.
4. H. SEIDEL and L. CSERPREGI, *Sensors and Actuators* (1983) 455.
5. R. FRANK, *Sensors and Actuators A* **28** (1991) 93.
6. M. BAO, L. YU and Y. WANG, *ibid.* **28** (1991) 105.
7. L. D. CLAYTON, E. P. EERNISSE, R. W. WARD and R. B. WIGGINS, *Sensors and Actuators*, **20** (1989) 171.
8. J. S. DANEL, F. MICHEL and G. DELAPIERRE, *ibid.* **A21-A23** (1990) 971.
9. K. E. PETERSEN, *Proc. IEEE* **70** (1982) 420.
10. K. SANGWAL, "Etching of crystals" (North-Holland, Amsterdam, 1987).
11. H. SEIDEL, L. CSEPREGI, A. HEUBERGER and H. BAUMGARTEL, *J. Electrochem. Soc.* **137** (1990) 3613.
12. C. R. TELLIER and S. DURAND, in Proceedings of the 9th European Frequency and Time Forum, Besançon, France, March 1995 (Imprimerie du Conseil Général du Doubs, 1995) pp. 426–489.
13. H. L. OFFEREINS, K. KUHL and H. SANDMAIER, *Sensors and Actuators A* **25-27** (1991) 9.
14. B. PUERS and W. SANSEN, *ibid.* **21-23** (1990) 1036.
15. Y. KANDA, *ibid.* **28** (1991) 83.
16. S. DURAND and C. R. TELLIER, *J. Phys. III* **6** (1996) 237.
17. Y. KANDA and A. YASUKAWA, *Sensors and Actuators* **2** (1982) 283.
18. Y. KANDA, *IEEE Trans. Electron Devices* **ED-29** (1982) 64.
19. S. DURAND and C. R. TELLIER, *J. Phys. III* **6** (1996) 237.
20. T. G. LEBLOIS, C. R. TELLIER and R. BOURQUIN, *Rev. Phys. Appl.* **24** (1989) 877.
21. P. VIGOUREUX and C. F. BOOTH, " Quartz vibrators and their applications," (HMSO, London, 1950).
22. R. J. JACCODINE, *J. Appl. Phys.* **33** (1962) 2643.
23. D. F. WEIRAUCH, *ibid.* **46** (1975) 1478.
24. D. W. SHAW, *J. Crystal Growth* **47** (1979) 509.
25. R. A. BUSER and N. F. DE ROOIJ, *Sensors and Actuators A* **28** (1991) 71.
26. C. R. TELLIER and T. G. LEBLOIS, in Proceedings of the IEEE Frequency Control Symposium, Salt Lake City, USA, June 1993 (IEEE, New York, 1993) pp. 397–406.
27. C. R. TELLIER and D. BENMESSAOUDA, in Proceedings of the 8th European Frequency and Time Forum, Munich, Germany, March 1994 (VDI Projekt, Dusseldörf, 1994) pp. 245–255.
28. C. R. TELLIER, *J. Crystal Growth* **96** (1989) 450.
29. C. R. TELLIER and J. L. VATERKOWSKI, *J. Mater. Sci.* **24** (1989) 1077.
30. C. R. TELLIER, J. Y. AMAUDRUT and A. BRAHIM-BOUNAB, *ibid* **26** (1991) 5585.
31. C. R. TELLIER and A. BRAHIM- BOUNAB, *ibid.* **29** (1994) 5953.
32. *Idem., ibid.* **29** 6354.
33. E. BASSOUS and E. F. BARAN, *J. Electrochem. Soc.* **125** (1978) 1321.
34. K. E. BEAN, *IEEE Trans. Electron Devices* **ED-25** (1978) 1185.
35. L. CSEPREGI, *Microelect. Engng.* **3** (1985) 221.
36. A. BRAHIM- BOUNAB and C. R. TELLIER, in Proceedings of 6th European Frequency and Time Forum, Noordwick, The Netherlands, March 1992 (European Space Agency, Paris, 1992) pp. 349–354.
37. R. B. HEIMANN, in Silicon chemical etching, edited by J. Grabmaier (Springer, Berlin, 1982) pp. 197–224.
38. B. A. IRVING, in "The electrochemistry of semiconductors," edited by P. J. Holmes (Academic Press, London, 1962) p. 256.
39. X. P. WU and W. H. KO, *Sensors and Actuators* **18** (1989) 207.
40. S. DURAND, PhD thesis, Université de Franche Comté, Besançon, France (1995).
41. T. G. LEBLOIS and C. R. TELLIER, *J. Phys. III* **2** (1992) 1259.
42. C. R. TELLIER, A. BRAHIM- BOUNAB and J. Y . AMAUDRUT, *J. Mater. Sci.* **26** (1991) 5594.
43. G. K. MAYER, H. L. OFFEREINS, H. SANDMAIER and K. KUHL, *J. Electrochem. Soc.* **137** (1990) 3947.

Received 23 July 1996
and accepted 17 April 1997